Dense arrays of millimeter-sized glass lenses fabricated at wafer-level

Jorge Albero,[1,*] Stéphane Perrin,[1] Sylwester Bargiel,[1] Nicolas Passilly,[1] Maciej Baranski,[1] Ludovic Gauthier-Manuel,[2] Florent Bernard,[1] Justine Lullin,[1] Luc Froehly,[2] Johann Krauter,[3] Wolfgang Osten,[3] and Christophe Gorecki[1]

[1]Dept. of Micro Nano Sciences and Systems, Institut FEMTO-ST (UMR CNRS 6174, Université de Franche-Comté), 15B avenue des Montboucons, F-25030 Besançon, France
[2]Dept. of Optics, Institut FEMTO-ST (UMR CNRS 6174, Université de Franche-Comté), 15B avenue des Montboucons, F-25030 Besançon, France
[3]Institut für Technische Optik, Universität Stuttgart, Pfaffenwaldring 9, D-70569 Stuttgart, Germany
[*]jorge.albero@femto-st.fr

Abstract: This paper presents the study of a fabrication technique of lenses arrays based on the reflow of glass inside cylindrical silicon cavities. Lenses whose sizes are out of the microfabrication standards are considered. In particular, the case of high fill factor arrays is discussed in detail since the proximity between lenses generates undesired effects. These effects, not experienced when lenses are sufficiently separated so that they can be considered as single items, are corrected by properly designing the silicon cavities. Complete topographic as well as optical characterizations are reported. The compatibility of materials with Micro-Opto-Electromechanical Systems (MOEMS) integration processes makes this technology attractive for the miniaturization of inspection systems, especially those devoted to imaging.

OCIS codes: (220.3630) Lenses; (230.3990) Micro-optical devices; (350.3950) Micro-optics.

References and links

1. V. Lin, H.-C. Wei, H.-T. Hsieh, and G.-D. J. Su, "An optical wavefront sensor based on a double layer microlens array," Sensors **11**, 10293-10307 (2011).
2. A. Moini, "Image Sensor Architectures," in *Smart Cameras*, A. N. Belbachir, ed. (Springer, 2013).
3. S. Bargiel, C. Gorecki, M. Barański, N. Passilly, M. Wiemer, C. Jia, and J. Froemel, "3D micro-optical lens scanner made by multi-wafer bonding technology," Proc. SPIE **8616**, 861605 (2013).
4. D. Kuang, X. Zhang, M. Gui, and Z. Fang, "Hexagonal microlens array fabricated by direct laser writing and inductively coupled plasma etching on organic light emitting devices to enhance the outcoupling efficiency," Appl. Opt. **48**(5) 974-978 (2009).
5. Z. Popovic, R. Sprague, and G. A. N. Conell, "Technique for monolithic fabrication of microlens arrays," Appl. Opt. **27**(7), 1281-1284 (1988).
6. D. Daly, R. F. Stevens, M. C. Hutley, and N. Davies, "The manufacture of microlenses by melting photoresist," Meas. Sci. Technol. **1**, 759-756 (1990).
7. H. Yang, C.-K. Chao, M.-K. Wei, and C.-P. Lin, "High fill-factor microlens array mold insert fabrication using a thermal reflow process," J. Micromech. Microeng. **14**, 1197–1204 (2004).
8. C.T. Pan, C.H. Su, "Fabrication of gapless triangular micro-lens array," Sensor Actuat. A-Phys. **134**, 631-640 (2007).
9. J. Albero, L. Nieradko, C. Gorecki, H. Ottevaere, V. Gomez, H. Thienpont, J. Pietarinen, B. Päivänränta, and N. Passilly, "Fabrication of spherical microlenses by a combination of isotropic wet etching of silicon and molding techniques," Opt. Express **17**(8), 6283-6292 (2009).
10. N. F. Borrelli, D. L. Morse, R. H. Bellman, and W. L. Morgan, "Photolytic technique for producing microlenese in photosensitive glass," App. Opt. **24**(16), 2520-2525 (1985).
11. M. Fritze, M. B. Stern, and P. W. Wyatt, "Laser-fabricated glass microlens arrays," Opt. Lett. **23**(2) 141-143 (1998).
12. G. Beadie and N. M. Lawandy, "Single-step laser fabrication of refractive microlenses in semiconductor-doped glasses," Opt. Lett. **20**(21), 2153-2155 (1995).
13. A. Y. Smuk and N. M. Lawandy, "Direct laser fabrication of dense microlens arrays in semiconductor-doped glass," J. Appl. Phys. **87**(8), 4026-4030 (2000).

14. M. Wakaki, Y. Komachi, and G. Kanai, "Microlenses and microlens arrays formed on a glass plate by use of a CO_2 laser," Appl. Opt. **37**(4), 627-631 (1998).
15. C. H. Lin, L. Jiang, Y. H. Chai, H. Xiao, S. J. Chen, and H. L. Tsai, "Fabrication of microlens arrays in photosensitive glass by femtosecond laser direct writing," Appl. Phys. A **97**, 751-757 (2009).
16. D. Nieto, J. Arines, C. Gomez-Reino, G. M. O'Connor, and M. T. Flores-Arias, "Fabrication and characterization of microlens arrays on soda-lime glass using a combination of laser direct-write and thermal reflow techniques," J. Appl. Phys. **110**, 023108 (2011).
17. F. Chen, Z. Deng, Q. Yang, H. Bian, G. Du, J. Si, and X. Hou, "Rapid fabrication of a large-area close—packed quasi-periodic microlens array on BK7 glass," Opt. Lett. **39**(3), 606-609 (2014).
18. S. Scheiding, A. Yi, A. Gebhardt, L. Li, S. Risse, R. Eberhardt, and A. Tünnermann, "Freeform manufacturing of a microoptical lens array on a steep curved substrate by use of a voice coil fast tool servo," Opt. Express **19**(24), 23938-23951 (2011).
19. P. Savander, "Microlens arrays etched into glass and silicon," Opt. Laser Eng. **20**(2), 97-107 (1994).
20. T. Knieling, M. Shafi, W. Lang, and W. Benecke, "Microlens array production in a microtechnological dry etch and reflow process for display applications," J. Eur. Opt. Soc.-Rapid **7**, 12007 (2012).
21. A. Sayah, V. K. Parashar, and M. A. M. Gijs, "Micro-replication of optical lenses in glass using a novel sol gel technology, in *Proceedings of IEEE Conference on Micro Electro Mechanical Systems* (IEEE, 2002), pp. 516-519.
22. T. Kreuzberger, A. Harnisch, M. Helgert, L. Erdmann, and R. Brunner, "Sol–gel process to cast quartz glass microlens arrays," Microelectron. Eng. **86**, 1173-1175 (2009).
23. M. He, X.-C. Yuan, N. Q. Ngo, J. Bu, and V. Kudryashov, "Simple reflow technique for fabrication of a microlens array in solgel glass," Opt. Lett. **28**(9), 731-733 (2003)
24. J. A. Dziuban, "Bonding" in *Bonding in Microsystem Technology*, K. Itoh, T. Lee, T. Sakurai, W. M. C. Sansen, D. Schmitt-Landsiedel, ed. (Springer-Verlag, 2006).
25. Y. Chen, A. Y. Yi1, D. Yao, F. Klocke, and G. Pongs, "A reflow process for glass microlens array fabrication by use of precision compression molding," J. Micromech. Microeng. **18**, 055022 (2008).
26. C.-Y. Huang, W.-T. Hsiao, K.-C. Huang, K.-S. Chang, H.-Y. Chou, and C.-P. Chou, "Fabrication of a double-sided micro-lens array by a glass molding technique," J. Micromech. Microeng. **21**, 085020 (2011).
27. P. Merz, H. J. Quenzer, H. Bernt, B. Wagner, and M. Zoberbier, "A novel micromachining technology for structuring borosilicate glass substrates," in *Proceedings of IEEE Conference on Solid State Sensors, Actuators and Microsystems*, (IEEE, 2003), pp. 258-261.
28. J. Albero, L. Nieradko, C. Gorecki, H. Ottevaere, V. Gomez, and J. Pietarinen, "Si moulds for glass and polymer microlenses replication," Proc. SPIE **6992**, 69920A (2008).
29. S. Yoo, J.-G. Ha, J.-Y. Jin, C.-H. Ji, and Y.-K. Kim, "Monolithically integrated glass microlens scanner using a thermal reflow process," J. Micromech. Microeng. **23**, 065012 (2013).
30. J. Albero, S. Bargiel, N. Passilly, P. Dannberg, M. Stumpf, U. D. Zeitner, C. Rousselot, K. Gastinger, and C. Gorecki, "Micromachined array-type Mirau interferometer for parallel inspection of MEMS," J. Micromech. Microeng. **21**, 065005 (2011).
31. J. Krauter, T. Boettcher, W. Osten, W. Lyda, N. Passilly, L. Froehly, S. Bargiel, J. Albero, S. Perrin, J. Lullin, and C. Gorecki, "Optical Design of a Vertically Integrated Array-type Mirau-based OCT system," Proc. SPIE **9132**, 91320L (2014).
32. J. Albero, C. Gorecki, L. Nieradko, B. Päivänranta, V. Gomez, H. Thienpont, and N. Passilly, "Matrixes of unconventional micro-optical components molded with etched silicon," J. Eur. Opt. Soc.-Rapid **5**, 10001 (2010).
33. M. Baranski, N. Passilly, J. Albero, and C. Gorecki, "Fabrication of 100% fill factor arrays of microlenses from silicon molds," Proc. SPIE **8428**, 84281G (2012).
34. A. Schilling, R. Merz, C. Ossmann, and H.P. Herzig, "Surface profiles of reflow microlenses under the influence of surface tension and gravity," Opt. Eng. **39**(8), 2171-2176 (2000).
35. *Thermal properties of Borofloat®33* in http://www.schott.com/borofloat/english/attribute/thermic/index.html
36. M. Baranski, S. Perrin, N. Passilly, L. Froehly, J. Albero, S. Bargiel, and C. Gorecki, "A simple method for quality evaluation of micro-optical components based on 3D IPSF measurement," Opt. Express **22**(11), 13202-13212 (2014).
37. *Borofloat®33 Temperature dependence of the viscosity* in http://www.schott.com/borofloat/english/attribute/thermic/index.html
38. D. Wu, Q.-D. Chen, L.G. Niu, J. Jiao, H. Xia, J.-F. Song, and H.-B. Sun, "100% fill-factor aspheric microlens arrays (AMLA) with sub-20-nm precision," IEEE Photonic. Tech. L. **21**, 1535-1537 (2009).
39. H. Ottevaere, R. Cox, H. P. Herzig, T. Miyashita, K. Naessens, M. Taghizadeh, R. Völkel, H. J. Woo, and H. Thienpont, "Comparing glass and plastic refractive microlenses fabricated with different technologies," J. Opt. A - Pure Appl. Op. **8**(7), 407-429 (2006).
40. H. Scholze, *Glass: Nature, Structure and Properties*, (Springer-Verlag, 1991).

1. Introduction

The technology of microlenses fabrication has been the inner workings of many research groups all around the world for the last two decades. Nevertheless, when it comes to integration of microlenses in complex microsystems, the realizations become less numerous, although today it is among the most needed features of microoptics. Nowadays, optical microsystems are conceived so that their architecture includes one or more microlenses. It is not only the case for scientific-oriented applications such as wavefront sensing [1], smart pixel cameras [2], or integrated microscopy [3], but also for everyday life products, e.g., organic light emitting diodes (OLED) outcoupling efficiency enhancement [4] or mobile devices photo cameras. The integration of microlenses rises the important question about what material should be employed. Factors such as the application, the illumination wavelength or the environment where microlenses will be used, determine whether they should be made of plastic or glass. On the one hand, when dealing with refractive microlenses, the first choice is usually preferred since many polymer techniques have been developed so far, hence reaching high optical quality. Some of them are very well mastered for wafer-level fabrication, namely polymer reflow [5,6] and its numerous variants and evolutions [7,8], whereas other techniques are adapted for mass fabrication, i.e., microinjection molding, UV molding or hot embossing [9]. On the other hand, although their fabrication might be more challenging, glass microlenses offer some clear advantages, e.g., better aging and suitability for harsh environments in terms of mechanical and thermal shocks. The first realizations based on photosensitive glass were reported already in the 80's [10]. Laser glass melting allowed the fabrication of good quality microlenses with high numerical apertures (NA) in standard glass [11] and also in semiconductor-doped glass [12,13]. These techniques evolved by relying on different lasers wavelengths and types of glass [14], and more recently with the use of femtosecond lasers [15], with the combination of laser and thermal glass reflow [16] or combined with wet etching [17]. Diamond micromachining process is precise but less time efficient. Indeed, it is generally used to fabricate molds instead of microlenses in glass directly on a substrate [18]. Other approaches profit from the polymer microlenses fabrication techniques that are eventually transferred into glass, e.g., by dry etching [19,20] but at the expense of a reduced optical quality. Different fabrication strategies based on solgel materials can be found in the literature [21,22], some of them being analogous to polymer reflow fabrication techniques [23].

Among all the existing techniques, the ones for which microlens arrays are directly fabricated in the substrate help avoiding refraction index matching issues and mechanical stress at the interface between different materials. In this framework, borosilicate glass is an excellent candidate for microlenses integration in Micro-Opto-Electro-Mechanical Systems (MOEMS) thanks to its compatibility with silicon processing regarding thermal expansion properties. Indeed, silicon-based MOEMS require specific assembly methods, usually involving high temperatures and mechanical stress. For this purpose, a well-known example of monolithic integration of microcomponents is based on the association of borosilicate glass and silicon assembled by anodic bonding [24], usually performed at temperatures over 300°C. Therefore, techniques involving glass allow wafer level fabrication [25,26] and some of them can be used when microlenses must be monolithically integrated with silicon [27-29].

Generally, most of these techniques are reported for the fabrication of microlenses having diameters under 1 mm. However, applications often related to optical metrology of large areas (few millimeters) demand integrated microlenses having diameters and NA over the standards of microsystems. An example is the parallel inspection system of MEMS and MOEMS reported in [30], where microlenses with diameters over 2 mm and NA over 0.1 are vertically assembled. Also, integrated parallel inspection systems devoted to biomedical applications present similar or more demanding needs. To achieve high performances, these systems are designed with large apertures (around 2 mm) and arranged in dense matrices [31]. This is due to the need of inspecting relatively large zones, which is achieved by stitching the acquisition from adjacent channels. To ensure the success of these miniature devices, the fabrication

technique must combine, in addition to the size and material requirements, the integration possibility, high fill factors and the best achievable optical quality. The vast majority of existing fabrication techniques are limited, either because of the available aperture diameters or due to the technological limitations to achieve sufficient NA.

The first suited technique could be diamond turning. Although its ability to deliver high quality microlenses is demonstrated, it is rarely used to directly machine glass. Moreover, parallel approach, high NA and high fill factors could be limiting factors, especially when dealing with miniaturized systems aiming reduced costs by batch fabrication. The same considerations can be applied to laser glass melting. Additional candidate could be glass molding from silicon masters since monolithic integration is practically straightforward, thus highly compatible with MOEMS technologies [28]. Although homogeneous matrices of spherical microlenses can be created with high fill factors [32], there is a limited trade-off between the microlens diameter and its available NA [33].

In here, we consider the Glass Flow Process (GFP) which was first reported by Merz *et al*. [27] where sub-millimeter diameters microlenses were fabricated. In this process, a glass substrate located on top of cylindrical silicon cavities is heated so that it melts. Convex shapes are obtained in a similar manner than during polymer reflow [34] although they are the consequence of forces due to pressure difference and glass viscosity. This process can be suited for dense matrices of plano-convex microlenses generation and, as it will be in here demonstrated, millimetric sized lenses generation with good optical quality is possible.

Consequently, we show in the following how to proceed in order to fabricate plano-convex glass lenses arrays that fulfill the requirements of millimeter-range diameters, high NA and high fill factors. Although this technique can already be used when single lenses are needed, the fabrication of dense arrays of millimeter-sized lenses introduces additional effects that need to be identified and controlled. A study of issues linked to the proximity and location of each lens on the array is detailed and fabricated samples under different conditions are presented, characterized and discussed.

2. Lenses generation

2.1 Fabrication

Single or dense arrays of plano-convex glass millimeter-sized lenses share the main technological steps (Fig. 1). First, the silicon cavities are generated by spin-coating a 2.5 µm thick layer of SPR220 3.0 photoresist on a 4", 500 µm thick silicon substrate. The latter is patterned by standard UV photolithography to define the footprint of the lenses, i.e., the diameter and pitch in the array (Fig. 1(a)). Note that the main differences between the single case and array case concern the design of the photolithography mask, as it will be shown in the following sections. Silicon is etched anisotropically (perpendicularly to the wafer surface) through the mask apertures by deep reactive ion etching (DRIE) with a Pegasus Rapier ICP DRIE system from SPTS (Fig. 1(b)). The depth of the obtained cylindrical cavities is fixed to 250 µm. The photoresist is afterwards removed with acetone in an ultrasound wet bench and decontaminated with a piranha solution (H_2O_2:H_2SO_4, 1:4).The Si wafer is rinsed in deionized water and processed with a CL200 megasonic cleaner (Süss Microtech), where it is again rinsed and dried by infrared lamps while spinning. A 4" wafer of Borofloat®33 (Schott) follows the same cleaning procedure and anodic bonding is performed under vacuum environment ($1.8 \cdot 10^{-3}$ mbar) at 350°C with an EVG501 equipment (Fig.1(c)). Special attention is given on the quality of the Si-glass anodic bonding since non-bonded zones around the silicon cavities could be responsible of thermal differences and, at the end, shape and size deviations in the matrix. After careful inspection, no defects nor voids are visible on the bonded surfaces. As it will be seen, the obtained results demonstrate that anodic bonding quality is sufficient. Such Si-glass stack is subsequently introduced in a furnace (oxidation tube, AET Technologies). The temperature is then raised at a speed of 20°C/minute until a value between the annealing and the softening point of Borofloat®33 (560°C and 820°C, respectively [35]), in order to deform the glass substrate toward the bottom of the Si cavities.

At such temperatures, the process is basically governed by the ideal gas law $P\,V=n\,R\,T$, where P is the pressure, V is the volume, n is the amount of substance of gas, R is the ideal gas constant and T is the absolute temperature of the gas. The high pressure difference between the cavity and the outside is sufficient to avoid an equilibrium situation, so that the cavity would be completely filled by glass after a sufficiently long time. However, with a precise control of time, the process can be stopped when the glass surface is deformed towards the bottom of the cavity in order to create the convex side of the lens (Fig. 1(d)). Control over time instead of pressure is preferred since the latter would require to accurately setting a weak vacuum level, in the order of 10^{-1} mbar, in the anodic bonding chamber. Such pressure accuracy is not easy to obtain and control, especially since the pressure sensing is not performed within the cavities.

This surface, formed without any contact with silicon, will be the convex side of the final lens. Its *saggita* (sag) is then controlled by the time spent inside the furnace at a temperature between 600 and 700°C. It can be noted that once the sag value is reached, melting must be slowed down by a relatively abrupt temperature drop. Indeed, natural cooling would let the glass reflow continue for undetermined time and rate. However, this thermal shock could also induce stresses at the Si-glass interface and result eventually in excessive wafer bowing. The latter would be very inconvenient since the flat side of the plano-convex lenses is obtained after glass grinding and polishing and it would lead to local thickness deviations. Consequently, once the viscosity of glass is sufficiently high again (at a temperature around 600°C), the cooling speed is reduced to allow structural relaxation and thus avoid local microcracking and eventual local crystallizations. Therefore, after reaching the targeted sag, the substrates are kept at 560°C during several hours so that the interface stresses can be minimized.

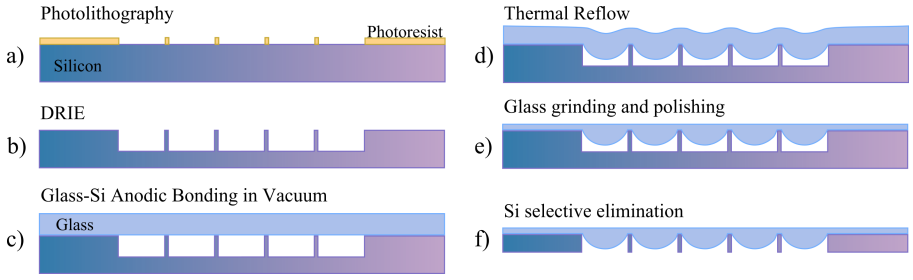

Fig. 1. Glass millimeter-sized lenses process flowchart at wafer level.

After all the thermal steps are concluded, the glass backside is grinded down to the desired thickness and polished to obtain optical quality surface with a Logitech PM5 equipment (Fig. 1(e)). To release the convex side of the lenses (Fig. 1(f)), several options can be suitable, depending on the target application. For example, unnecessary silicon can be removed by DRIE. But even with a fine control of the process, this option might degrade the surface quality of the lenses. Indeed, the cavities depth is expected to vary over the whole wafer and some lenses will be facing the plasma before all of them are released. Wet anisotropic etching of silicon with low-concentrated solutions of KOH or TMAH is another option (Fig. 2(a)). Although the damage on the convex surface would be lower, the process would be undoubtedly much longer and glass backside protection becomes mandatory. Another alternative concerns silicon grinding-and-polishing in the same manner as the glass backside. It offers a higher degree of protection of the lenses and it has the advantage of providing high quality surface when remaining silicon is needed (Fig. 2(b)). The latter becomes very convenient when vertical integration of the lenses on a multicomponents microsystem is involved, allowing additional anodic bonding post-processing.

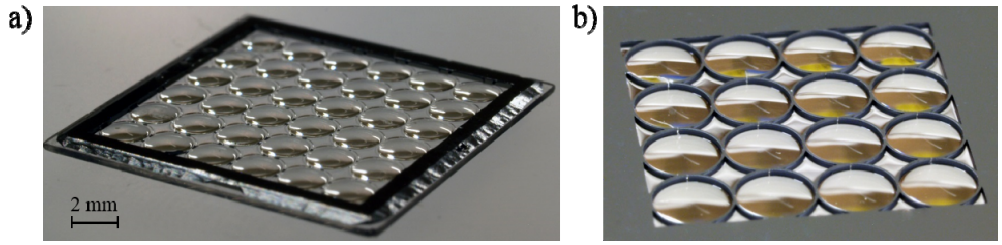

Fig. 2. Microfabricated glass lenses, a) completely released by wet etching and surrounded by a silicon frame, b) silicon is selectively eliminated by grinding and polishing for vertical integration purposes. Lenses on both arrays are the same size.

2.2 Array considerations

Following this flow-chart, preliminary runs of lens matrices fabrication have shown significant non-uniformities over matrices. In addition, compared to single lenses, those arranged in matrices ended up with stronger asymmetries that seemed related to the arrangement and the positions of neighboring components. Sag variations up to 20% have been measured between lenses of the same array.

In this work, we consider square arrays of 1.9 mm apertures with a 2 mm pitch. When working with matrices, it is obvious that the deviation of parameters between lenses must be minimal. Thus, additional optimization strategies need to be implemented. A major side effect encountered when dense matrices are designed concerns the *neighboring*. When generating single lenses, the boundary conditions do not change in the proximity of each cavity, which produces rotationally symmetric volumes of glass after reflow. In an array, these conditions change dramatically due to the variations of the *glass share*, which can be understood as the available amount of glass to fill the cavities. Each item is closely surrounded by other lenses, and in a square arrangement, the distances between cavities at 0° and 90° are equal but different from the one at 45°. This breaks the spherical symmetry of the reflowed glass. The worst case happens with the cavities at the edges of the matrix, since the number of adjacent cavities varies. In addition, different thermal evolutions during heating and/or cooling could be expected since each cavity plays an insulation role. Since the viscosity varies exponentially with temperature, differences as small as several degrees could be responsible for significant sag variations. Optically, the sum of these effects leads to sag variation over matrices and astigmatism for each lens. Two strategies have been tested to counter these effects. The first one, straightforward, consists on simply adding an extra set of cavities surrounding the matrix of interest but to be discarded for use (for example, the 4x4 central array in the arrangement of Fig. 2(a) improves uniformity with respect to the one in Fig. 2(b)). It solves the problem of the amount of adjacent lenses (thermal conditions are similar from one lens to another). Complementarily, the second strategy consists in demarcating each cavity by only a ring with a thickness equal to the minimum distance between cavities, as it can be seen in Fig. 2(b). Therefore, the amount of silicon surrounding each cavity is constant. One has to be aware that this strategy will add smaller cavities in between lenses, where glass undergoes a reflow as well. Contribution of such additional refractive surfaces to the lens matrices should then be cancelled, via proper masking or illumination structuration. The ideal case is the combination of both strategies, so that the *glass share* and thermal conditions can be equivalent for all central lenses of the array. As it will be shown in the following section that reports on optical characterization, the optical performance is strongly degraded when none of the exposed effects are taken into account, whereas non-uniformity and asymmetry are not anymore experienced when correcting strategies are implemented.

3. Characterization and discussion

To characterize the process in different conditions, several Si-glass bonded wafers were saw-diced prior to the high temperature processing. Samples of 15x15 mm^2 were obtained, each of

them containing a matrix of 6x6 sealed cavities. The samples were individually introduced in a furnace at temperatures set between 625°C and 700°C in steps of 25°C for different amounts of time. After reflow, topography of at least one of the central lenses per matrix was characterized with a MSA-500 (Polytec) equipment. The measured profiles were then fitted by paraboloidal (conic constant k = -1) or spherical functions to evaluate the maximum usable diameter for a given wavefront deterioration. Finally, optical performances were characterized in transmission by evaluating the 3D intensity point spread function (IPSF) [36].

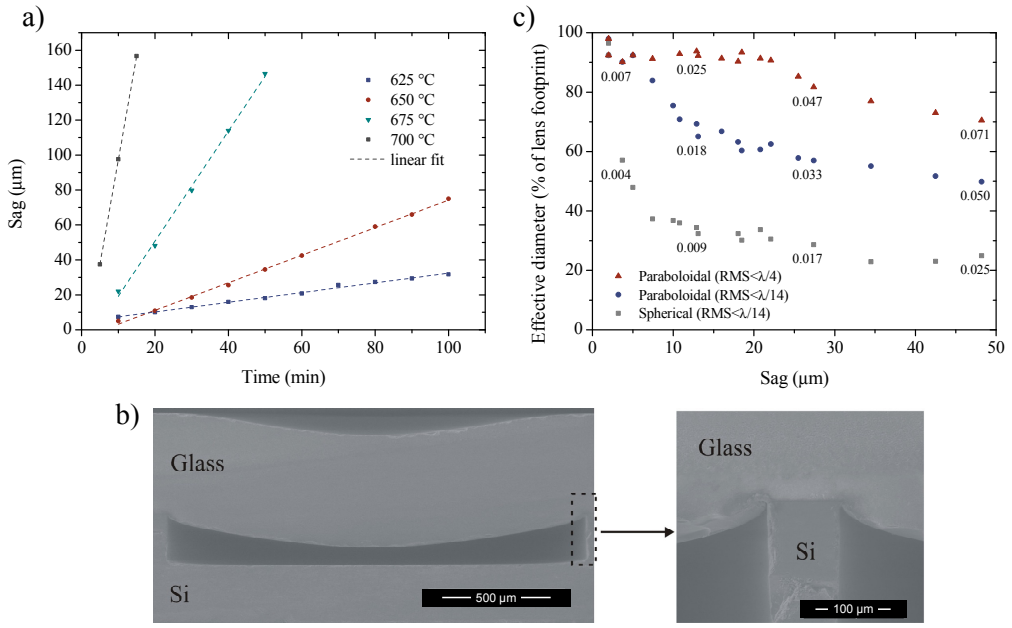

Fig. 3. a) Measured sag as a function of time for different glass reflow temperatures. All groups of values are linearly fitted; b) image of the transverse cut of a lens on a 6x6 matrix after glass reflow and prior to the grinding and polishing of its backside, and a detailed view of the 100 µm-wide Si ring and the *piston* effect, with the radius of curvature varying near the lenses' edge; c) percentage of the maximum diameter of fabricated lenses providing a certain level of optical performances as a function of their sag.

Figure 3(a) shows the evolution of sag with time as a function of reflow temperatures. As it was expected, the higher the temperature, the faster the sag variation, due to the much lower viscosity at 700°C compared to the one at 625°C (namely, $10^{9.5}$ vs $10^{11.3}$ dPas, respectively) [37]. It can be underlined that in this range of temperatures, the sag evolution over time is linear with slopes depending on the viscosity. In here, note that *Time=0* corresponds to the moment when the set temperature is reached, i.e. the steady thermal state. For *Time <0*, temperature is raised at a rate of 20°C/minute. In steady thermal state, it can be seen how linearity is the common behavior at tested temperatures with a coefficient of determination R^2>0.99 in all cases. This indicates that the forces (generated by pressure difference on the one hand and resistance through viscosity on the other hand) remain constant over time. Since the temperature fixes the viscosity, the pressure difference has to stay constant while the membrane deflects, i.e., enclosed pressure must remain small regarding external pressure although the cavity volume changes. If we consider linear sag evolution over time, pressure changes due to depth differences between cavities (e.g. resulting from DRIE non-uniformity) are very unlikely to be responsible for sag deviations. In here, cavities are 250µm deep. In such a case, cavity pressure increases during reflow, reaching values 4 times higher than initial ones, but it remains small compared to external pressure to have any influence on suction force. In addition, etching much deeper cavities than targeted sags allows a wider range of silicon frame thicknesses as well as an easier lens releasing. Regarding sag deviations

instead, thermal conditions are very likely to be responsible because of exponential dependence of viscosity with temperature. The fact that surrounding cavities generate convex surfaces with different sag is attributed to slight temperature differences during transient regimes (heating and cooling steps) between glass and silicon, resulting in turn to temperature difference of glass at distinct locations within matrix. In this sense, the two implemented strategies are intended to improve the uniformity of thermal conditions for inner lenses. For a high accuracy of the process, low temperatures should be preferred, especially when low sag is aimed whereas temperatures over 675°C might compromise the sag control. The precision is successfully achieved at temperatures under 675°C, not only between similarly processed 15x15 mm^2 samples but also compared to full 4" wafers. The obtained sag differs by less than 2 µm with respect to the target values. The samples for this work are fabricated at 625°C, 650°C and 675°C. An important effect over sag is the *piston* behavior, which can be defined as a translation of the lens edges toward the bottom of the cavity. As it can be seen in Fig. 3(b), the radius of curvature changes at the borders. Since the process is based on glass viscous flow, we can consider that the *piston*-like edge profile is due to a lateral movement of the glass close to the boundary.

The topography of lenses fabricated under different parameters, namely temperature and time of reflow, was fitted both with a spherical and a parabolic profile in order to evaluate the percentage of the initial diameter where the lenses offer good optical performances (maximum effective diameter). Results of fitting are shown in Fig. 3(c), where the abscissa axis represents the absolute sag of the measured lens and NA values produced by the effective diameter are superimposed to each series. Figure 3(c) proves that, rather than spherical, this fabrication technique provides parabolic profiles. This is consistent with the flow-driven mechanism interpretation for which the shape is more likely to be parabolic. Moreover, it reduces spherical aberrations and is sometimes preferred [38]. The fabricated lenses could only be considered spherical by greatly reducing usable diameter, i.e. the diameter corresponding to the largest illuminated area to stay diffraction limited. In terms of uniformity, sag deviations of ±0.2 µm have been measured on the 4x4 central items of the 6x6 arrays. With such low deviation, resolution variations within a matrix are negligible and, in terms of focal length, the spread is small compared to the depth of focus for the values that can be reached with this technique. For instance, for a 100 µm-sag lens matrix, range of focal lengths would be within ±0.2%. In our characterizations, two scenarios were distinguished to qualify the lenses. First, the diffraction limit is defined according to the Maréchal criterion (root mean square –RMS– wavefront error < λ/14). This criterion, used in exhaustive characterization of microlenses [39] gives a limit usable diameter of about 50% of the real diameter of the fabricated lenses, corresponding to NA=0.05 and about 70% for NA=0.02. If the conditions are relaxed to the Rayleigh criterion (RMS wavefront error < λ/4, considered sometimes in micro-optics qualification), the usable aperture diameter increases to about 80% for equivalent NA=0.05 and 90% for NA=0.02. These values of NA are of interest for a specific OCT application working at a wavelength of λ=850 nm [31]. Note that the fitting was reported only for lenses having sag<60 µm due to the limited NA of the MSA-500 optical profilometer. It is important to point out that much higher sag can be obtained with this technique compared to the majority of reported techniques, although a reduction of the effective diameter should be envisaged to keep an optically reliable performance.

In order to evaluate the true optical performances of the lenses and not only derived from their topography, the 3D IPSF [36] of lenses from different matrices was additionally measured in transmission mode and compared with the case of standard matrices (without compensation) and with the case of a single lens of equivalent dimensions. Let us consider first the performances of the lenses matrices where the neighboring effects are compensated. For the sake of fair comparison, Fig. 4(a) shows the normalized intensity 2D beam profile (transversal cut) at the focal plane of four lenses L*i* (*i*=1,..,4), having sags equal to 80, 115, 150 and 180 µm. Each lens belonged to the central part of a 6x6 matrix. The 3D IPSF was recorded by illuminating the lens with a laser operating at λ=632.8 nm using the transmission mode of the setup described in [36]. For this measurement, a 950 µm aperture stop is placed

just before the lens to illuminate the best quality zone in all cases, i.e, 50% of the lens diameter. Considering the NA of each lens as

$$\mathrm{NA} \approx \frac{2\mathrm{D}}{f'} \tag{1}$$

where D represents the illuminated area diameter and f' is the focal length of the lens, the associated NA of each Li are 0.039, 0.056, 0.072 and 0.086, respectively. Table 1 lists the values of measured beam full width at half maximum ($\mathrm{FWHM_{meas}}$) from the 3D IPSF analysis, as well as the expected value for each lens from geometric parameters, calculated as

$$\mathrm{FWHM_{geo}} = 0.51\frac{\lambda}{\mathrm{NA}} \ . \tag{2}$$

Measured values are close to the theoretical ones, although this simple model considers only spherical shapes and does not take into account aberrations. Figure 4(b) shows the longitudinal cut where the presence of spherical aberrations is noticed by the lobes appearing before the focal plane.

Table 1. Measured and calculated values of FWHM.

	L1	L2	L3	L4
$\mathrm{FWHM_{meas}}$ (µm)	8.1	6.8	3.5	3.4
$\mathrm{FWHM_{geo}}$ (µm)	8.2	5.7	4.4	3.6

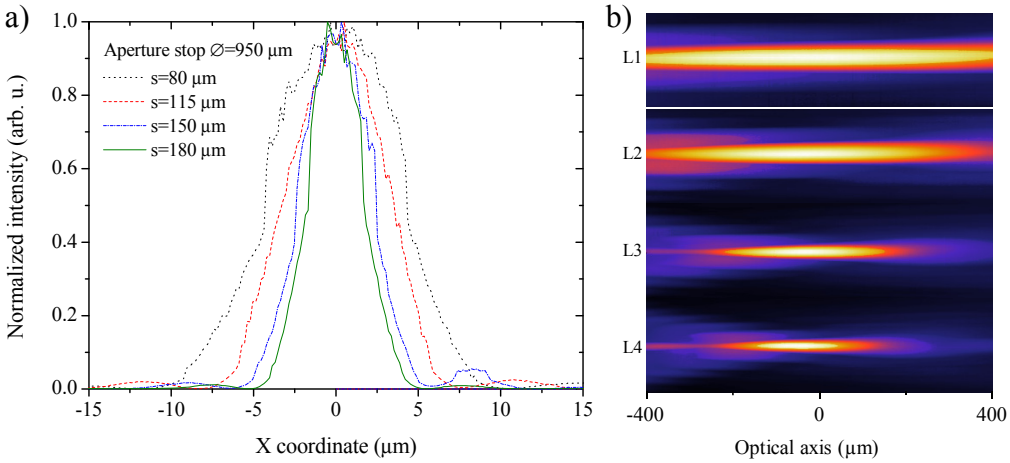

Fig. 4. IPSF measurement of the beam near the focal plane of lenses having sag of 80, 115, 150 and 180 µm (L1 to L4, respectively), each one belonging to 6x6 independent matrices: a) transverse beam profiles in the focal plane and b) false color longitudinal profiles of the same beams (range of the vertical scale is 50 µm for each image).

As it is stated in [40], a high temperature thermal treatment of glass could produce a reduction of its refraction index. Indeed, taking L3 as an example, illumination through a 950 µm aperture leads to an equivalent sag of 35.3 µm, meaning a radius of curvature ROC=3083 µm. Based on the thin lens approximation, its focal length f' can be defined as

$$f' = \frac{\mathrm{ROC}}{(\mathrm{n}-1)}, \tag{3}$$

where Borofloat®33 specified index of refraction n=1.470 at λ= 632.8 nm would lead to a value of 6560 µm. However, the focal length of L3 was measured to be f'=6850±70 µm,

taking into account the uncertainty due to the depth of focus. This higher value could be attributed to a reduction of the refraction index, which would then be equal to 1.450±0.004 if the change were considered uniform. Similar refractive index reduction was already reported for heated borosilicate glass [40]. Nevertheless, it is unlikely that the refractive index change remains uniform and radial variation of the glass density may be foreseen. Hence, to evaluate the presence of an index-of-refraction variation, we compared topography measurements of the convex side and transmission measurements. To look for refractive index changes over the largest available area, a 42 µm sag and 1.9 mm diameter lens (L5) was chosen in order to obtain the topography without numerical aperture limitations of the measurement system. Therefore, the presence of refractive index changes can be evaluated on an area only limited by the field of view of the topography system. As shown in Fig. 5(a), the retrieved phase (blue line - calculated with an iterative phase retrieval algorithm using Fourier images generated by the lens) differs from the expected phase resulting from an optically uniform material of n_{border} having the shape of L5 (dashed line – derived from topography measurements). The slightly shallower phase profile corresponds to a longer measured focal length. Since the plano-side of the lens was measured to be flat ($<\lambda/20$), the difference is attributed to a radial variation of the glass refractive index. Figure 5(b) shows the 2D map of the index of refraction of L5 retrieved from the same measurements. As it can be seen, it is reduced radially towards the center of the lens until a value of 1.445. It can be noted that refractive index values are averaged along the propagation axis through the lens, i.e., given values are just estimated but they explain the longer measured focal length with respect to the one derived from the topography. Although uniformity of refractive index is a major concern of glass reflow processes, the experienced repeatability of results on different fabrication runs show that these deviations can be anticipated in design. The index of refraction variation could be due to several reasons. The insights of Si-glass anodic bonding are based on the application of an electric field between both substrates at elevated temperatures (around 350°C). This implies a Na^+ ions migration in the glass towards the electrode (in opposite direction to the silicon-glass interface) and a depletion layer generation at the Si-glass interface rich in O^- and OH^- ions. Due to the size of the cavities, a difference in ion migrations at the borders of the lens compared to its center could be expected and thus, a variation of the index of refraction. Another reason could concern the high temperature treatment of glass. Borosilicate glasses are basically composed of solid phases of SiO_2 and B_2O_3 but they also contain a certain amount of other different compounds depending on the manufacturer. The glass melting in a cavity could lead to local concentrations of these compounds and thus varying the index of refraction. Finally, the glass located at the center of the cavity (sealed under vacuum) might be more thermally insulated and it would accumulate more heat. These effects are the subjects of a subsequent study to be published elsewhere.

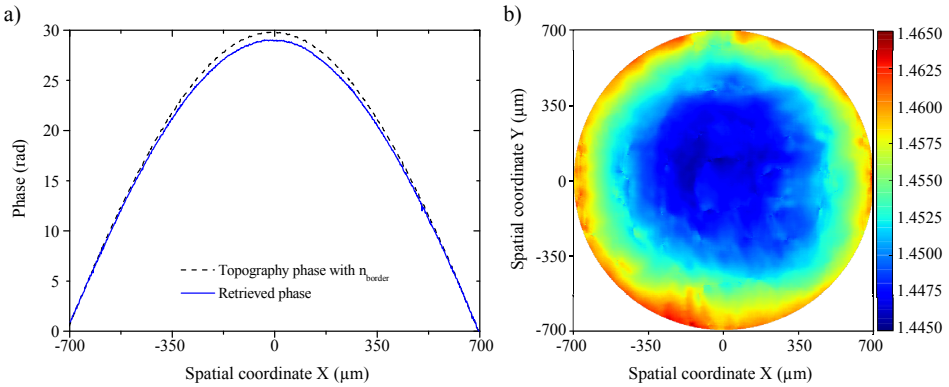

Fig. 5. Refraction index variation of L5 after thermal processing of glass inside the silicon cavity, a) transverse profile variation of the phase retrieved from the 3D IPSF compared to the estimated phase profile obtained from the topography, the latter considering a constant refraction index value measured at the lens' edge n_{border}.; b) 2D map of the refraction index.

Regarding the roughness of the lenses surface, the fact that the convex side is obtained with a contactless process ensures a high surface quality, equivalent to that of the bulk glass wafer. The flat side of the lenses was polished with colloidal silica of about 30 nm diameter to achieve optical surface quality.

Figure 6 shows the measured 2D MTF with the same characterization bench [30] as a function of the resolved frequencies on the XY plane (considering Z the optical axis) of the same type of lens in the three tested different situations, namely a single lens, and two lenses in matrices where compensation strategies are applied or not. It is important to mention that all three lenses sags are in the same range (±10 µm), with the same diameter and illuminated through the same 950 µm aperture stop, so that differences can be attributed mostly to the neighboring effects. Contour lines at different values are traced for a better visibility of symmetry deviations. In the first case, a single lens where no neighboring effect is applicable shows a highly symmetric MTF (Fig 6(a)). The second one shows the MTF of a lens in a matrix compensated for the neighboring effects (Fig 6(b)). Although a slight deformation of the symmetry can be noticed, it is clearly better than the third case, corresponding to a lens in a matrix where no compensation is applied, i.e., circular apertures in a square arrangement (Fig 6(c)). Insets in Fig. 5 show a detail of each photolithography mask design, where white zones represent not etched silicon.

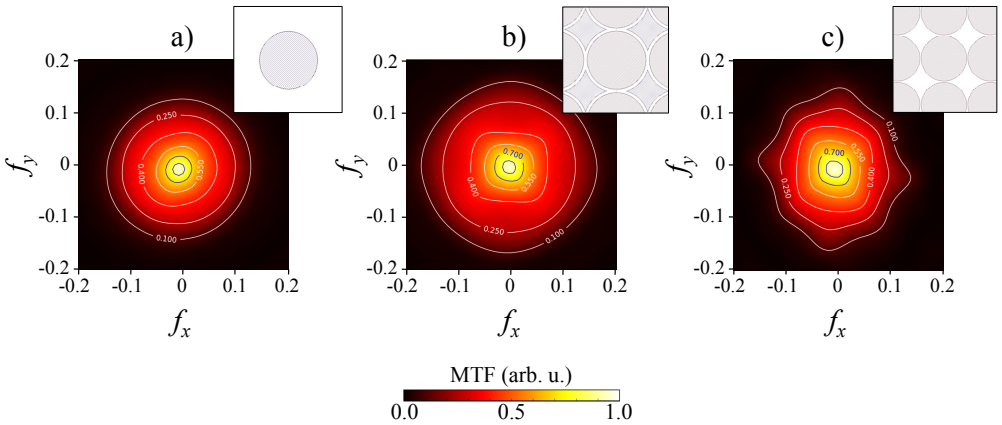

Fig. 6. Measured 2D MTF of glass millimeter-sized lenses in different situations, a) single item, b) square array with applied compensation strategies and c) square array without compensation. Vertical and horizontal axes represent resolved frequencies, normalized to 2NA/λ. Contours are traced at contrasts equal to 0.1, 0.25, 0.4, 0.55, 0.7 and 0.85.

4. Conclusions

In this paper, we studied the fabrication of glass, millimeter-sized, parabolic lens arrays at wafer level by glass reflow processing. The effects induced by proximity between lenses and their positioning in a matrix are studied and solutions to the main issues are proposed. Extended characterizations have been performed in order to estimate the capabilities of the fabricated lenses to provide diffraction-limited optical performances. This technique allows large diameters and numerical apertures around 0.1 with high accuracy. The nature of the process makes these glass lenses great candidates for monolithic integration in microsystems whose architecture requires parameters out of the standards of microfabrication.

Acknowledgments

This work has been realized in the framework of the VIAMOS collaborative project, funded under the Grant Agreement 318542 to the 7th Framework of the European Union. This work was supported in part by the French RENATECH network and its FEMTO-ST technological facility MIMENTO and also by Labex ACTION of FEMTO-ST (ANR-11-LABX-0001-01).